Optical polarization evolution and transmission in multi-Ranvier-node myelin sheath waveguides

Emily Frede[1,2,3]**, Hadi Zadeh-Haghighi**[1,2,3]**, and Christoph Simon**[1,2,3]

[1]Department of Physics and Astronomy, University of Calgary, Calgary, AB T2N 1N4, Canada
[2]Institute for Quantum Science and Technology, University of Calgary, Calgary, AB T2N 1N4, Canada
[3]Hotchkiss Brain Institute, University of Calgary, Calgary, AB T2N 1N4, Canada
[*]corresponding.author@email.example
[+]these authors contributed equally to this work

ABSTRACT

In neuroscience it is compelling to consider all possible information transfer between neurons, in order to fully understand processing in the brain. It has been suggested that photonic communication may be possible along axonal connections, especially through the myelin sheath as a waveguide due to its high refractive index. There is already a good deal of theoretical and experimental evidence for light guidance in the myelin sheath despite realistic optical imperfections, however the feature of light polarization remains largely unexplored. Polarization evolution is relevant to our interest in considering neural communication via the exchange of biophotons, which have been observed in the brain predominantly within the visible spectral range. It is presently unclear whether polarization-encoded information could be preserved within the myelin sheath. We simulate propagation of a single-wavelength mode through a myelinated axon structure with multiple Ranvier nodes. This allows us to observe polarization change and test the assumption of exponentiated transmission loss through multiple Ranvier nodes for guided light along myelin sheath waveguides. These results provide important context for information transmission facilitated by biophotons, leaving open the possibilities of both classical and quantum photonic communication within the brain.

Introduction

The brain is a complex system of billions of neurons, which are structurally interconnected by axons. It is well-known these axonal connections facilitate electrochemical signals between neurons in the form of action potentials. However, there are many unanswered questions remaining in neuroscience[1], notably with regards to mechanisms of higher-order functions such as learning[2], memory[3,4], and consciousness[5–7]. Difficulties that have arisen in understanding these higher-order functions may indicate that electrochemical signals are not the only modality of information processing in the brain. It has been proposed that additional information transfer may be orchestrated through the exchange of biophotons between neurons[8–10], especially along myelinated axons as waveguides[11–13] due to the high refractive index of myelin[14].

Biophotons are produced within the wavelength range of 350 nm – 1300 nm by oxidative processes in living cells[15]. Their estimated rate of production is on the order of 1 - 10,000 photons per second per centimeter of tissue squared[15] – though this rate might be higher inside cells[16]. They have been observed in a range of organisms and tissues[15], and their spectral range is affected by species[17] and the aging process[18]. Their existence in the brain is well-established[15,19–23], and their activity between neurons can be considered as a potential means of information transfer. There are indications photons may play a role in cellular communication generally[24]. It is argued that biophoton production is a good candidate for encoding information[9], as their originating oxidative processes also produce reactive oxygen species which are known to be strongly regulated cellular signals in biological systems[25–28]. In an *in vivo* examination of rat brain, biophoton emission intensity was shown to be correlated with neural activity through EEG techniques[20] which indicates emission may be meaningful. Photons serving as information carriers could have many functions within neural information processing, e.g., facilitating backpropagation, a well-known mechanism for learning, within the brain[29].

Photonic communication in the brain would have unique features due to the nature of biophotons[9,12]. While biophoton signal speed would depend on emission and detection rates, photons travel at the speed of light and therefore such signals could potentially be very fast relative to the electrochemical processes for action potentials. These signals would likely face very little background noise[15], since the biophotons predominantly exist in the visible spectral range which is distinct from the blackbody radiation due to internal body temperature. Furthermore, biophotonic signals would be able to communicate information in multiple ways – by photon number, frequency, and polarization. Since photon polarization can encode quantum information,

biophoton signals leave the possibility open for quantum communication in the brain[11, 12, 30]. So, it seems pertinent to assess if effective transmission of biophotons in the brain environment is a biologically realistic phenomenon. The myelin sheath as a waveguide is a plausible mechanism for long-range biophoton transmission between neurons[11].

There are a number of experimental studies that support the plausibility of light guidance along myelinated axons. In particular, a recent study[31] demonstrates a clear directional dependence on light transmission across myelinated axons, finding a 50% decrease in scattering power for light propagation along highly myelinated and organized (spinal cord) white matter tracts. In contrast, directional dependence in overall light attenuation did not occur in grey matter where there is very little myelin and myelin organization. Images from this experimental study also show increased transmission through the myelin sheath in comparison to the axon, further highlighting the importance of the myelin sheath to light guidance along nerve fibers. These findings confirm prior indirect evidence[32] for light conduction along white matter tracts. Other experimental studies have also observed increased biophoton activity at the end of nerve roots in response to light stimulation[8] and at axons and axon terminals in response to glutamate stimulation[23]. So it seems plausible for biophotons in particular to travel along myelinated axons.

Myelinated axons are the predominant nerve fibers found in white matter, which makes up about half of the human brain[33]. On such axons, the myelin sheath envelopes the axon as an insulating lipid layer which increases the propagation speed of action potential signals[34]. The myelin sheath therefore inherits bends and cross-sectional shape from the axon, and is interrupted at regular intervals by nodes of Ranvier which are vital for its function in speeding up action potentials[35]. In the central nervous system, myelin is formed by the oligodendrocyte glial cells. Light guidance in the myelin sheath would not be a new function for glial cells, as Müller cells are known to guide light in mammalian eyes[36, 37]. It is also known that the myelin sheath is not a static structure, which naturally affects its properties as a waveguide. Myelination is a plastic process, such that axons become myelinated and myelin sheaths can undergo structural changes (e.g., changes in thickness, internodal lengths, Ranvier node geometry, etc.) throughout the entire lifetime[38].

The first study simulating myelin sheath waveguides was conducted by Kumar, et al. in 2016[11], which assessed whether myelinated axons can serve as biophoton waveguides despite realistic optical imperfections. They simulated (biophoton spectral range) mode propagation through models of myelinated axon segments, informed by biologically-observed optical properties, finding transmitted light to be well-confined to the myelin sheath. Their models assessed light transmission in the context of imperfections that can interfere with light-guiding ability, most notably a Ranvier node, bends in the axon, varying myelin sheath thickness, and non-circular nerve fiber cross-sections. Their treatment to estimate transmission across entire inter-neuron distances demonstrated that biophoton transmission along myelinated axons is possible within realistic expectations of these optical imperfections. This has sparked various theoretical studies[13, 39–44], and the possibility of myelin sheath waveguides has been well-supported through subsequent simulations. Another biophoton-motivated simulation study[13] considered (optical spectral range) mode propagation in the context of a myelinated axon model containing the detailed multi-lamellar structure of the myelin sheath. They found an optimum of low attenuation and low dispersion within realistic parameters of this model for light near operating wavelengths in the biophoton wavelength range. Dependence in operating wavelength due to axon diameter and myelin thickness, especially as may be implemented by myelination plasticity, may well explain spectral redshift of biophotons in species[17] and blueshift during the aging process[18].

Other theoretical approaches to investigate myelin sheath light guidance utilise an idealized representation of the myelinated axon in order to obtain electromagnetic field solutions. For this simple model in the context of the optical and infrared spectral range, it has been demonstrated analytically that localized weakly damped modes can exist in myelinated axons[40]. It has also been recognized that the cross-section of myelinated nerve fiber can be thought of as a depressed-core fiber due to its refractive index profile. Myelinated nerve fiber can be treated as an anti-resonant reflecting optical waveguide[39] (a model developed for depressed-core fibers[45]) wherein myelin, as the high-index cladding, acts as a Fabry-Perot cavity and will confine and transmit incident light well even in the presence of optical imperfections.

We study how a guided mode propagates through the structure of the myelinated axon by observing polarization evolution and transmission through multiple Ranvier nodes. To our knowledge, this is the first work considering the evolution of light polarization in the myelin sheath. In Methods we describe our myelinated axon model, informed by biological observations, and software details as they pertain to our findings. In Results we present observations of polarization evolution and transmission of a guided mode through the myelinated axon model with four Ranvier nodes. Significance of results, suggested improvements to the model, and applications are discussed. We also briefly present calculations of the modes of the myelin sheath in Appendix A, and preliminary polarization and transmission results of mode propagation in the birefringent myelin sheath in Appendix B. Additional figures to observe polarization evolution in the myelin sheath are included in Supplemental Information.

Methods

This section details the construction of our myelinated axon model, and discusses relevant software details and settings as they pertain to our results. ANSYS Lumerical FDTD: 3D Electromagnetic Simulator software[46] is used for model construction and simulation of light propagation.

Model design

Input light and material optical properties

To simulate biophotons as the light source, we specify wavelength to be $\lambda = 0.4\,\mu$m. This falls within the biophotonic spectral range[15] of $0.35\,\mu$m – $1.3\,\mu$m. We choose to restrict our input light to a single (short) wavelength within this range in order to offset computational demands of the simulation software. Shorter wavelengths can be well-confined in myelinated axons having thinner myelin with correspondingly smaller cross-sectional dimensions, which decreases the simulation region volume required to contain the model.

We take the myelinated axon to be composed of three fundamental materials: axon, myelin sheath, and interstitial fluid. These are all modelled as uniform dielectric materials of specified refractive index. We set refractive indices to $n_a = 1.38$ for the axon[47], $n_m = 1.44$ for the myelin sheath[14], and $n_{int} = 1.34$ for the interstitial fluid[48] as consistent with biological observations. This refractive index profile highlights the high refractive index of the myelin sheath, which underpins its waveguiding ability.

We also theorize that our choice of wavelength, and the larger biophoton spectral range, faces negligible absorption by the myelin sheath over inter-neuron distances on the centimeter scale as previously discussed[11]. The myelin sheath is composed of lipids, proteins, and water. In consideration of lipids, we recognize that mammalian fat has a very low absorption coefficient (less than $0.01\,\mathrm{mm}^{-1}$) for the biophoton spectral range[49]. Water has a similarly low absorption coefficient. Most proteins, similar to what is found in the myelin sheath, have negligible absorption for wavelengths around $0.34\,\mu$m and above[50]. The conjecture of low biophoton absorption in the myelin sheath is also indirectly supported by studies on brain tissue. Absorption in white matter is relatively low (its absorption coefficient decreasing almost monotonically from $\sim 0.3\,\mathrm{mm}^{-1}$ to $\sim 0.07\,\mathrm{mm}^{-1}$ over the wavelength range of $0.4\,\mu$m – $1.1\,\mu$m), wherein the presence of myelin is thought to have little effect as grey matter has comparable absorption coefficients[51]. Observations have also shown that optical attenuation in brain tissue is primarily due to scattering and not absorption[52].

Myelinated axon structure

The biological axon (also referred to as a nerve fiber) is roughly cylindrical in shape, located in an environment of interstitial fluid. We model the myelinated axon to have an ideal cylindrical structure with specified dimensions. We take the symmetry of axis to be the z axis, which coincides with the propagation direction of the input light. The only z dependence in the model is due to the Ranvier nodes, the myelin sheath being present in the internodal regions and absent in the nodal regions.

Internodal regions feature the axon and surrounding myelin sheath as illustrated from multiple perspectives in Fig. 1, for which we now describe the cross-section. An inner cylinder of radius r_a models the axon. An outer cylindrical ring of inner radius r_a and outer radius r_m models the myelin sheath. The ratio between r_m and r_a is known as the g-ratio, such that $r_a = g \cdot r_m$. We take $g = 0.6$ which is close to the experimental average[53]. As we have chosen $\lambda = 0.4\,\mu$m for our input light, we set the myelin thickness $t = r_m - r_a = 0.4\,\mu$m. This ensures good confinement for the light within the myelin sheath while ensuring computational demands are manageable. Taken together with the g-ratio, this corresponds to an axon radius of $r_a = 0.6\,\mu$m. This is consistent with the biologically observed values of axon diameter which are between $0.2\,\mu$m – $10\,\mu$m in cortical white matter[54]. So, we set axon radius $r_a = 0.6\,\mu$m and myelin radius $r_m = 1\,\mu$m.

Ranvier nodes, segments of bare axon with no myelin sheath, interrupt internodal regions at regular intervals. They are a critical feature to consider when assessing the ability of the myelin sheath to serve as a waveguide, since this presents a significant opportunity for transmission loss. The Ranvier node is known to be roughly $1\,\mu$m - $2\,\mu$m in length[55,56]. In our model we set Ranvier node length to be $2\,\mu$m, such that the myelin sheath abruptly ends at these boundaries and its cross-section only includes that of the axon. In this work we do not model the paranodal regions, located at the boundaries between the internode and Ranvier node segments at which the constituent cytoplasmic loops of the myelin taper off onto the axon. There is significant variation in internode distance within the central nervous system, however internode distance has a strong relationship with the outer myelin diameter of the nerve fiber[53]. It has been observed that fibers with an outer myelin diameter of $2\,\mu$m (as in our case) roughly correspond to $100\,\mu$m in internode distances[53]. In our model we set the node-to-node distance to be $100\,\mu$m, such that the Ranvier node is $2\,\mu$m in length and the internode is $98\,\mu$m in length. Our myelinated axon model is $500\,\mu$m in length and includes four Ranvier nodes placed at $z = 100, 200, 300, 400\,\mu$m, as shown later in Fig. 2.
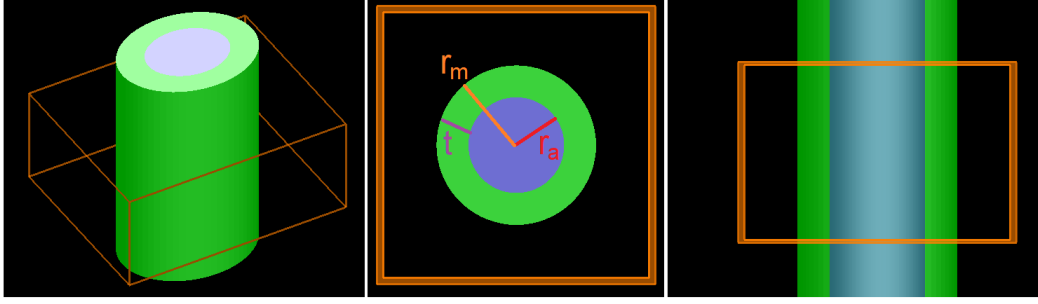
Figure 1. Internodal region of myelinated axon model. The blue area represents the axon, the green area represents the myelin sheath, the orange lines included to enhance perspective and to depict a test simulation region. Leftmost image depicts perspective view, center image depicts cross-section, rightmost image depicts side view. The cross-section of the internodal region is annotated with the axon radius r_a, the outer myelin radius r_m, and the myelin thickness t. Images taken from ANSYS Lumerical FDTD: 3D Electromagnetic Simulator software[46].

Software: Simulation Region and Monitors

This project utilised ANSYS Lumerical FDTD: 3D Electromagnetic Simulator software[46] (version: 8.26.2779) to construct models and run simulations. This software uses the Finite Difference Time Domain (FDTD) method[57] to solve Maxwell's equations for models on the nanometer scale, which allows us to calculate modes and simulate light propagation in our myelinated axon model. The FDTD method solves for the electric and magnetic field components on a discrete spatial and temporal grid within the Yee cell paradigm. For further details about software methods and simulation settings, see Supplementary Information.

We consistently set the simulation region to span $4\,\mu$m in the x and y directions so that the cross-section is square. These dimensions were chosen to generously allow more than a wavelength distance ($\lambda = 0.4\,\mu$m) between the outer myelin radius and the simulation boundary, after which we say light is lost to the external environment. The simulation region spans $500\,\mu$m in the z direction. The input mode is applied as a planar source placed at the beginning of the region at $z = 0\,\mu$m. The myelinated axon model is always centered in the simulation region cross-section and makes use of the entire length of the region to consider light propagation through multiple Ranvier nodes. All boundaries of this simulation region are set to PML (perfectly matched layer) which models perfect absorption and simulates complete loss of light at the boundaries.

In this work we collect transmission and electric field profile data at twenty cross-sectional monitors throughout the $500\,\mu$m length of the simulation region, which contains the myelinated axon structure having four Ranvier nodes. Monitors were located along the z axis with the same x and y boundaries as the simulation region (each spanning $4\,\mu$m). They were placed $25\,\mu$m apart, starting at $z = 25\,\mu$m and ending at $z = 500\,\mu$m. This was taken to be adequate sampling to observe changes in the electric field, being significantly smaller than the internodal length of $98\,\mu$m (as Ranvier nodes cause changes in the propagation of the light). The software automatically snaps these monitors to the location of the nearest mesh cell, designed to improve data accuracy by minimizing interpolation required. Monitors placed at boundaries of the nodes and at the boundary at the end of the simulation region may have some slight inaccuracies due to this interpolation.

Results

In this section, we simulate the propagation of a mode through the myelinated axon structure with four Ranvier nodes. This allows us to observe the electric field profile, both its magnitude and polarization, at different cross-sections throughout the structure. We present the input mode and the electric field profiles at $z = 75, 175, 275, 375, 475\,\mu$m in Fig. 7, which shows electric field behavior well after any given Ranvier node. Electric field profiles at a resolution of $25\,\mu$m are presented in Supplemental Information. Simulating light propagation here also allows us to characterize the transmission drop-off through multiple Ranvier nodes. Transmission as a function of distance along the myelin sheath is presented in a log-plot in Fig. 8.

The HE_{21}^o mode, shown in Fig. 3a – 3b, is used as the input mode for our four-Ranvier-node structure. The magnitude plot of this mode in Fig. 3a shows four high-magnitude areas we will refer to as anti-nodes, which are equally spaced and interspersed with low-magnitude nodes. The vector plot in Fig. 3b shows its hyperbolic polarization pattern. Input light amplitude is set to $100\,$V/m. We recognize that the modes of the myelinated axon structure have been calculated and examined in previous studies[13]. These are supported by mode calculations for our model. We present the first twelve modes calculated for

our myelinated axon model in Appendix A, to further highlight various polarization patterns of guided light in the ideal myelin sheath.

Our four-Ranvier-node myelinated axon structure is $500\,\mu$m long as shown in Fig. 2, measured along the z axis which is the symmetry axis for the model. Input light is applied at $z = 0\,\mu$m. Ranvier nodes are taken to be $2\,\mu$m gaps in the myelin sheath, located at $z = 100, 200, 300, 400\,\mu$m. While electric field and transmission results presented in the main text pertain to the case of uniform myelin sheath, we also model the biologically-measured radial birefringence of the myelin sheath and present the results in Appendix B. In the case of the birefringent myelin sheath, the electric field profile results are qualitatively similar, and the transmission drop-off through the Ranvier nodes is virtually identical.
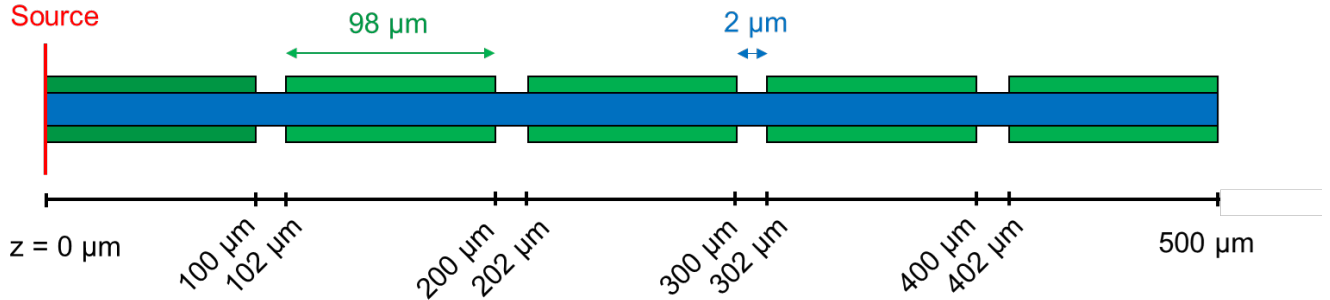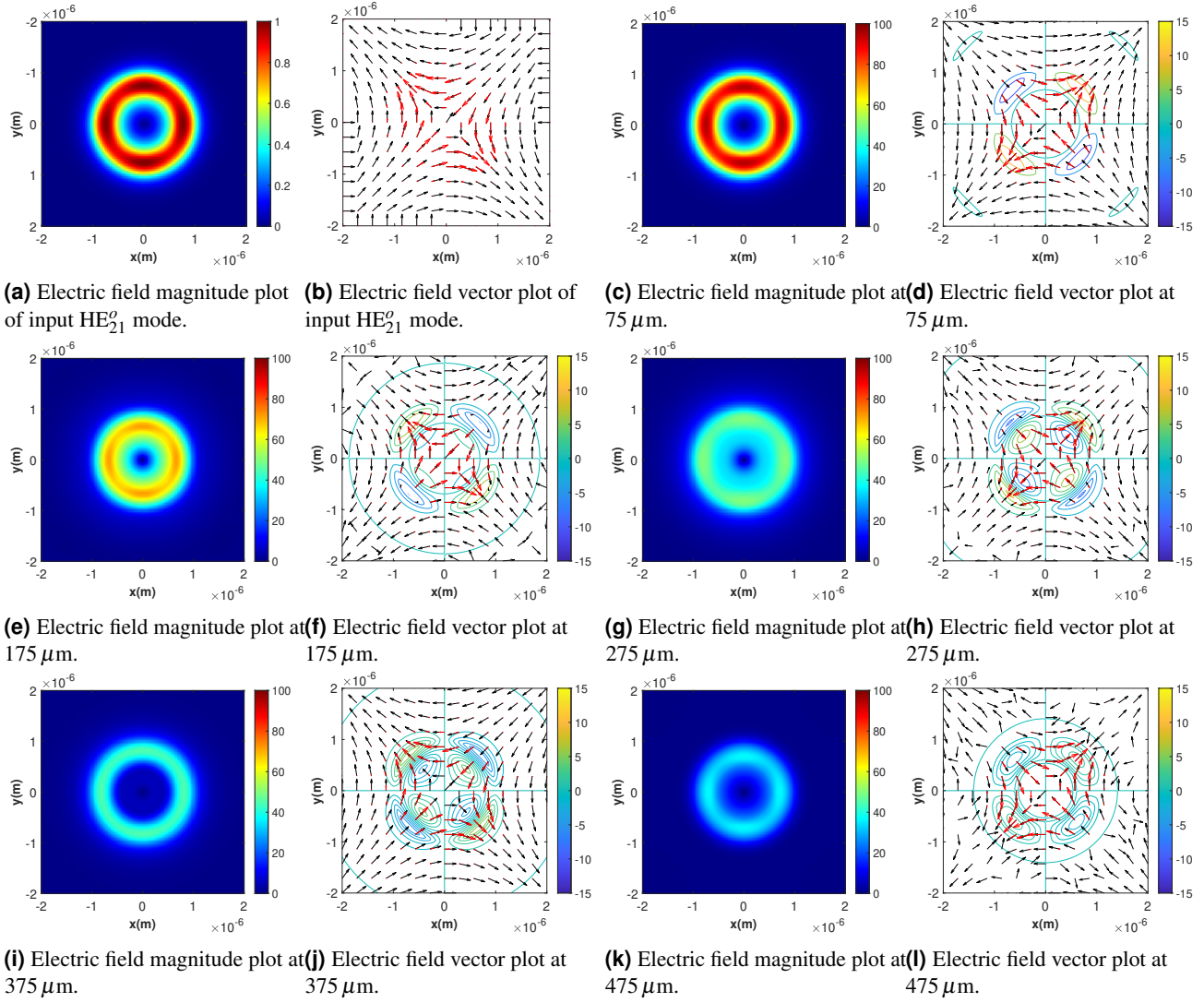

Figure 2. Longitudinal diagram of the four-node structure. The blue area represents the axon, the green areas represent the myelin sheath. The nodes are $2\,\mu$m in width, and are spaced $100\,\mu$m apart. Note that $z = 0\,\mu$m is the beginning of the simulation and location of the mode source, $z = 500\,\mu$m is the end of the simulation.
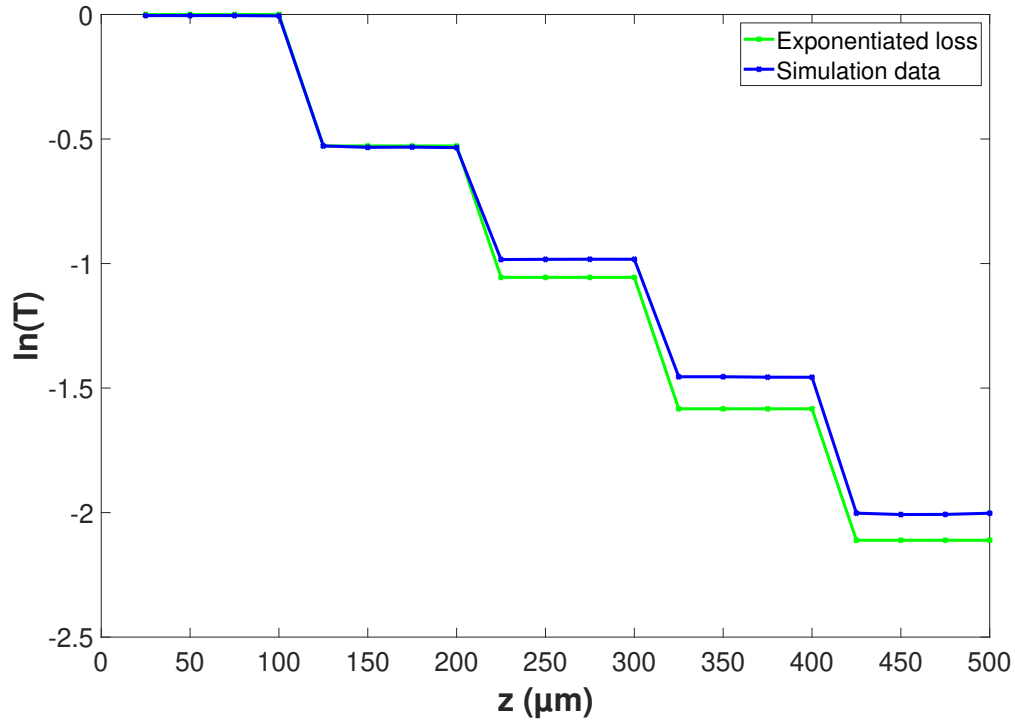
At $75\,\mu$m in the myelinated axon structure, the electric field profile is shown in Fig. 3c – 3d. This magnitude and vector plot at $75\,\mu$m, match those of the mode calculated at $0\,\mu$m. As expected, the mode remains confined to the myelin sheath and there is no observable change in its polarization. (The only noticeable change in the magnitude plots is the nonzero E_z component at $75\,\mu$m, in contrast to the calculated mode at $0\,\mu$m, due to the mode's forward propagation along the z axis.) It is also propagating with 100% transmission as expected, indicated in the transmission plot in Fig. 8 prior to the first node at $100\,\mu$m. At $175\,\mu$m, after the first Ranvier node, the electric field profile is shown in Fig. 3e – 3f. There is clearly a decrease in magnitude due to the Ranvier node, however we still see light confined to the myelin sheath and four high-magnitude anti-nodes. The hyperbolic polarization pattern still appears well-preserved in the myelin sheath. At $275\,\mu$m, after two Ranvier nodes, the electric field profile is shown in Fig. 3g – 3h. At this position the magnitude has been further reduced from the Ranvier nodes and we see more light propagating in the axon. The polarization still appears well-preserved. At $375\,\mu$m (after three Ranvier nodes) shown in Fig. 3i – 3j, and at $475\,\mu$m (after four Ranvier nodes) shown in Fig. 3k – 3l, we see similar trends. The magnitude plot evolves according to position, magnitudes generally decreasing due to loss caused by the Ranvier nodes but continuing to propagate within the myelin sheath. The hyperbolic polarization pattern appears to stay well-preserved within the myelin sheath, where there is still significant light transmission.

The transmission coefficient T was recorded every $25\,\mu$m along the z length of the myelinated axon structure, for the cross-sectional area of the simulation region ($4\,\mu$m x $4\,\mu$m). The natural log of T is plotted against z in Fig. 8, plotting recorded simulation data in blue. We see perfect transmission prior to $100\,\mu$m, meaning prior to the first Ranvier node, as expected from the input mode of the model. The four decreases in transmission occur at sample cross-sections directly after the four Ranvier nodes at $z = 100, 200, 300, 400\,\mu$m. We compare this data to the prior assumption that the transmission across successive Ranvier nodes drops off according to exponentiated transmission loss. The transmission loss plotted in green depicts the expected transmission loss with this assumption, using the transmission coefficient after the first Ranvier node ($T = 0.5899$ measured at $z = 125\,\mu$m). (If we did use this assumption, we could theorize that axons 1 mm long, which is realistic for interneurons in the brain[58], may have for instance ten Ranvier nodes and therefore a net transmission coefficient of $T = 0.5899^{10} = 0.0051$.) Our simulation results show slightly higher transmission through subsequent Ranvier nodes than expected with this assumption. Since the light propagates in different modes after a Ranvier node, this higher than expected transmission may be due to the filtering of high-loss modes in earlier Ranvier nodes. So the propagation we are observing through later Ranvier nodes may primarily be the transmission of low-loss modes.

(a) Electric field magnitude plot of input HE_{21}^o mode.

(b) Electric field vector plot of input HE_{21}^o mode.

(c) Electric field magnitude plot at 75 μm.

(d) Electric field vector plot at 75 μm.

(e) Electric field magnitude plot at 175 μm.

(f) Electric field vector plot at 175 μm.

(g) Electric field magnitude plot at 275 μm.

(h) Electric field vector plot at 275 μm.

(i) Electric field magnitude plot at 375 μm.

(j) Electric field vector plot at 375 μm.

(k) Electric field magnitude plot at 475 μm.

(l) Electric field vector plot at 475 μm.

Figure 3. Electric field profiles of calculated input mode HE_{21}^o and cross-sections of the four-Ranvier-node myelinated axon structure at positions $75, 175, 275, 375, 475 \, \mu$m. The mode source is located at $0 \, \mu$m, input amplitude is $100 \, \text{V/m}$. Ranvier nodes are $2 \, \mu$m long and begin at $z = 100, 200, 300, 400 \, \mu$m. Plots (a), (c), (e), (g), (i), (k) depict electric field magnitude. Plots (b), (d), (f), (h), (j), (l) depict electric field vectors; black lines depict the normalized three-dimensional electric field vector at a given position, red arrows depict the magnitude-scaled three-dimensional electric field vector at a given position; color-coded contour lines depict magnitude of E_z. Electric field magnitudes given in units of V/m.

Figure 4. Natural log of transmission coefficient T as a function of distance z along the four-Ranvier-node myelinated axon structure. The blue line shows transmission data collected from the simulation; the green line shows transmission data expected from the assumption of exponentiated loss through each Ranvier node, using the measured transmission loss from the first Ranvier node. The mode source is located at $z = 0\,\mu$m, Ranvier nodes are $2\,\mu$m long and begin at $z = 100, 200, 300, 400\,\mu$m.

Discussion

We have investigated the properties of guided light propagation in the myelin sheath with multiple Ranvier nodes, utilising ANSYS Lumerical FDTD: 3D Electromagnetic Simulator[46]. Our myelinated axon model was constructed according to biologically realistic structural and optical properties for axon, myelin sheath, and interstitial fluid material. We were able to observe polarization evolution and transmission at relatively long distances from the source, guided by the myelin sheath even in the presence of multiple Ranvier nodes. The polarization of the input mode appears qualiatively well-preserved through the four-Ranvier-node myelin sheath model, with high transmission within the myelin sheath. While it has been previously assumed[11] that light travelling through multiple Ranvier nodes may obey exponentiated transmission loss, results from our model show slightly higher transmission than this expectation. It may be the case that high-loss modes are filtered out through early Ranvier nodes, such that the transmission through later Ranvier nodes is primarily propagation of low-loss modes.

So far there are a number of limitations for this kind of model in its ability to describe potential biophoton travel through the myelin sheath. Consider the light source and detectors. For input light we use a single mode, which is applied by a planar source and simulates initial ideal transmission in the myelin sheath. This does not consider the point-like nature of biophotons and their sources, nor does it study how biophotons couple into the modes of the myelin sheath. Possible biophoton sources in neurons include mitochondria[59, 60] (mitochondrial respiration) and liposomes[61] (lipid oxidation). Mitochondria are particularly interesting as a potential source of biophotons in the context of a recent study[62] which indicates mitochondria are capable of encoding neuron firing frequency, as this could be a potential connection between action potential signals and biophoton signals. For light detectors, our study uses planar monitors to record electric field data for cross-sections of the myelinated axon model, however we would also expect biological biophoton detectors to be point-like in nature. Possible light-sensitive detectors in neurons include centrosomes[63] and chromophores within mitochondria[64]. Brain tissue is known to be light-sensitive in general[65–68], even containing light-sensitive opsin molecules within deep brain tissue[69].

We have considered polarization evolution and transmission in the myelin sheath through multiple Ranvier nodes. There are a number of features that can be added to our myelinated axon model to better describe the biological reality, as has been examined in previous studies[11, 13, 39] thus far to measure transmission through short segments of the myelin sheath. Polarization

evolution in the myelin sheath can be assessed across realistic ranges of biological parameters – notably axon radius, g-ratio, and biophoton wavelength – and in the presence of realistic optical imperfections such as bends in the axon, varying myelin thickness, irregular cross-section shapes and areas, and paranodal regions. We also recommend the positive radial birefringence of the myelin sheath[70,71] to be included appropriately in future models, especially for observations of polarization evolution.

Understanding how polarization evolves as light travels through the myelin sheath can help us determine if information encoded within polarization, such as might be encoded within biophoton information carriers, can be transmitted through these waveguides between neurons. If so, this allows the possibility of biophotonic quantum communication, as photon polarization is able to encode quantum information (in qubits) in addition to expected classical information (in bits). There is growing evidence that quantum effects may play significant roles in biological environments, including the brain[72]. It has been suggested[30] that the exchange of quantum information via biophotons might sustain an entangled system of spins within neurons in the brain. Quantum computation in the brain[73] may correspond to some quantum efficiency advantage, which is well-demonstrated in quantum computing for certain types of problems[74]. Efficiency would be a benefit to meet high computational demands of the brain under energy constraints within the body, especially for functions such as consciousness. Quantum entanglement may also play a role in consciousness, with the potential to well-explain its unified and complex nature[30,75]. So, understanding the nature of biophotons as possible information carriers, either classical or quantum in nature, may have many significant applications within the field of neuroscience.

There are a number of other motivations to characterize the optical properties of the myelin sheath, outside of possible biophotonic communication. The myelin sheath is also examined as a waveguide within the theory that Nodes of Ranvier act as relay amplifiers and produce infrared photons to facilitate saltatory conduction along myelinated axons[41–43,76]. We acknowledge this as a separate topic from guided biophotons along myelinated axons, considering a different spectral range with Ranvier nodes as sources. It also useful to characterize light interactions with the myelin sheath for the purposes of neuroimaging. Application of polarized light to brain tissue allows for 3D-PLI (3D polarized light imaging)[77,78] to image nerve fibers at a microscopic level. Entangled light might also be useful for imaging purposes[79,80]. It is important to consider how light interacts with neural cells in general, for applications in nanoscale optogenetics[81]. From a medical perspective, investigation of optical properties of the myelin sheath may lead to greater understanding of causes and potential treatments of diseases associated with it (such as multiple sclerosis[82]).

References

1. Adolphs, R. The unsolved problems of neuroscience. *Trends cognitive sciences* **19**, 173–175 (2015).

2. Humeau, Y. & Choquet, D. The next generation of approaches to investigate the link between synaptic plasticity and learning. *Nat. neuroscience* **22**, 1536–1543 (2019).

3. Sweatt, J. D. & Day, J. J. Dna methylation and memory formation. *Nat. neuroscience* **13**, 1319–1323 (2010).

4. Nadel, L., Hupbach, A., Gomez, R. & Newman-Smith, K. Memory formation, consolidation and transformation: Memory formation. *Neurosci. biobehavioral reviews* **36**, 1640–1645 (2012).

5. Koch, C., Massimini, M., Boly, M. & Tononi, G. Neural correlates of consciousness: progress and problems. *Nat. reviews. Neurosci.* **17**, 307–321 (2016).

6. Franks, N. P. General anaesthesia: from molecular targets to neuronal pathways of sleep and arousal. *Nat. reviews. Neurosci.* **9**, 370–386 (2008).

7. Mashour, G. A. Integrating the science of consciousness and anesthesia. *Anesth. & Analg.* **103**, 975–982 (2006).

8. Sun, Y., Wang, C. & Dai, J. Biophotons as neural communication signals demonstrated by in situ biophoton autography. *Photochem. photobiological sciences* **9**, 315–322 (2010).

9. Tang, R. & Dai, J. Biophoton signal transmission and processing in the brain. *J. photochemistry photobiology. B, Biol.* **139**, 71–75 (2014).

10. Liu, N., Wang, Z. & Dai, J. Intracellular simulated biophoton stimulation and transsynaptic signal transmission. *Appl. physics letters* **121**, 203701– (2022).

11. Kumar, S., Boone, K., Tuszyński, J., Barclay, P. & Simon, C. Possible existence of optical communication channels in the brain. *Sci. reports* **6**, 36508–36508 (2016).

12. Zarkeshian, P., Kumar, S., Tuszynski, J., Barclay, P. & Simon, C. Are there optical communication channels in the brain? (2017).

13. Zeng, H., Zhang, Y., Ma, Y. & Li, S. Electromagnetic modeling and simulation of the biophoton propagation in myelinated axon waveguide. *Appl. optics (2004)* **61**, 4013– (2022).

14. Antonov, I. P. *et al.* Measurement of the radial distribution of the refractive index of the schwann's sheath and the axon of a myelinated nerve fiberin vivo. *J. applied spectroscopy* **39**, 822–824 (1983).

15. Cifra, M. & Pospíšil, P. Ultra-weak photon emission from biological samples: Definition, mechanisms, properties, detection and applications. *J. photochemistry photobiology. B, Biol.* **139**, 2–10 (2014).

16. Bókkon, I., Salari, V., Tuszynski, J. & Antal, I. Estimation of the number of biophotons involved in the visual perception of a single-object image: Biophoton intensity can be considerably higher inside cells than outside. *J. photochemistry photobiology. B, Biol.* **100**, 160–166 (2010).

17. Wang, Z., Wang, N., Li, Z., Xiao, F. & Dai, J. Human high intelligence is involved in spectral redshift of biophotonic activities in the brain. *Proc. Natl. Acad. Sci. - PNAS* **113**, 8753–8758 (2016).

18. Chen, L., Wang, Z. & Dai, J. Spectral blueshift of biophotonic activity and transmission in the ageing mouse brain. *Brain research* **1749**, 147133–147133 (2020).

19. Ultraweak biochemiluminescence detected from rat hippocampal slices. *Neuroreport* **6**, 658–660 (1995).

20. Kobayashi, M. *et al.* In vivo imaging of spontaneous ultraweak photon emission from a rat's brain correlated with cerebral energy metabolism and oxidative stress. *Neurosci. research* **34**, 103–113 (1999).

21. Kataoka, Y. *et al.* Activity-dependent neural tissue oxidation emits intrinsic ultraweak photons. *Biochem. biophysical research communications* **285**, 1007–1011 (2001).

22. Wang, C., Bókkon, I., Dai, J. & Antal, I. Spontaneous and visible light-induced ultraweak photon emission from rat eyes. *Brain research* **1369**, 1–9 (2010).

23. Tang, R. & Dai, J. Spatiotemporal imaging of glutamate-induced biophotonic activities and transmission in neural circuits. *PloS one* **9**, e85643–e85643 (2014).

24. Fels, D. Cellular communication through light. *PloS one* **4**, e5086–e5086 (2009).

25. Kishida, K. T. & Klann, E. Sources and targets of reactive oxygen species in synaptic plasticity and memory. *Antioxidants redox signaling* **9**, 233–244 (2007).

26. Droge, W. Free radicals in the physiological control of cell function. *Physiol. Rev.* **82**, 47–95 (2002).

27. Bókkon, I. Recognition of functional roles of free radicals. *Curr. neuropharmacology* **10**, 287–288 (2012).

28. Miki, H. & Funato, Y. Regulation of intracellular signalling through cysteine oxidation by reactive oxygen species. *J. biochemistry (Tokyo)* **151**, 255–261 (2012).

29. Zarkeshian, P., Kergan, T., Ghobadi, R., Nicola, W. & Simon, C. Photons guided by axons may enable backpropagation-based learning in the brain. *Sci. reports* **12**, 20720–20720 (2022).

30. Simon, C. Can quantum physics help solve the hard problem of consciousness? *J. consciousness studies* **26**, 204–218 (2019).

31. DePaoli, D. *et al.* Anisotropic light scattering from myelinated axons in the spinal cord. *Neurophotonics (Print)* **7**, 015011–015011 (2020).

32. Hebeda, K. M., Menovsky, T., Beek, J. F., Wolbers, J. G. & van Gemert, M. J. Light propagation in the brain depends on nerve fiber orientation. *Neurosurgery* **35**, 720–724 (1994).

33. Buyanova, I. S. & Arsalidou, M. Cerebral white matter myelination and relations to age, gender, and cognition: A selective review. *Front. human neuroscience* **15**, 662031–662031 (2021).

34. Purves, D. *et al.* Increased conduction velocity as a result of myelination. *Neuroscience* (2001).

35. Arancibia-Cárcamo, I. L. *et al.* Node of ranvier length as a potential regulator of myelinated axon conduction speed. *eLife* **6** (2017).

36. Franze, K. *et al.* Müller cells are living optical fibers in the vertebrate retina. *Proc. Natl. Acad. Sci. - PNAS* **104**, 8287–8292 (2007).

37. Labin, A. M., Safuri, S. K., Ribak, E. N. & Perlman, I. Müller cells separate between wavelengths to improve day vision with minimal effect upon night vision. *Nat. communications* **5**, 4319–4319 (2014).

38. Periods of synchronized myelin changes shape brain function and plasticity. *Nat. neuroscience* **24**, 1508–1521 (2021).

39. Omidi, M., Zibaii, M. I. & Granpayeh, N. Simulation of nerve fiber based on anti-resonant reflecting optical waveguide. *Sci. reports* **12**, 19356–19356 (2022).

40. Ostafiychuk, O. M., Es'kin, V. A., Kudrin, A. V. & Popova, A. A. Electromagnetic waves guided by a myelinated axon in the optical and infrared ranges. In *2019 PhotonIcs Electromagnetics Research Symposium - Spring (PIERS-Spring)*, 1180–1184 (IEEE, 2019).

41. Zangari, A., Micheli, D., Galeazzi, R. & Tozzi, A. Node of ranvier as an array of bio-nanoantennas for infrared communication in nerve tissue. *Sci. reports* **8**, 539–539 (2018).

42. Liu, G. *et al.* Myelin sheath as a dielectric waveguide for signal propagation in the mid-infrared to terahertz spectral range. *Adv. Funct. Mater.* **29**, DOI: 10.1002/adfm.201807862 (2019).

43. Guo, L. *et al.* Electromagnetic characteristics of in vivo nerve fibers at the terahertz-far-infrared band. *Front. bioengineering biotechnology* **10**, 1055232–1055232 (2022).

44. Maghoul, A., Khaleghi, A. & Balasingham, I. Engineering photonic transmission inside brain nerve fibers. *IEEE access* **9**, 35399–35410 (2021).

45. Lian, X. *et al.* Anti-resonance, inhibited coupling and mode transition in depressed core fibers. *Opt. express* **28**, 16526–16541 (2020).

46. Ansys lumerical inc. (version: 8.26.2779) (2022).

47. Wang, Z. *et al.* Topography and refractometry of nanostructures using spatial light interference microscopy. *Opt. letters* **35**, 208–210 (2010).

48. Tuchin, V. V. *et al.* Light propagation in tissues with controlled optical properties. *J. Biomed. Opt.* **2**, 401–417 (1997).

49. Van Veen, R. *et al.* Determination of visible near-ir absorption coefficients of mammalian fat using time-and spatially resolved diffuse reflectance and transmission spectroscopy. *J. biomedical optics* **10**, 054004–054004 (2005).

50. Facci, P. *et al.* Kinetic and structural study of the interaction of myelin basic protein with dipalmitoylphosphatidylglycerol layers. *Biophys. J.* **78**, 1413–1419 (2000).

51. Yaroslavsky, A. *et al.* Optical properties of selected native and coagulated human brain tissues in vitro in the visible and near infrared spectral range. *Phys. Medicine & Biol.* **47**, 2059 (2002).

52. Cheong, W., Prahl, S. & Welch, A. A review of the optical properties of biological tissues. *IEEE journal quantum electronics* **26**, 2166–2185 (1990).

53. Friede, R. L. & Bischhausen, R. How are sheath dimensions affected by axon caliber and internode length? *Brain research* **235**, 335–350 (1982).

54. Liewald, D., Miller, R., Logothetis, N., Wagner, H.-J. & Schüz, A. Distribution of axon diameters in cortical white matter: an electron-microscopic study on three human brains and a macaque. *Biol. cybernetics* **108**, 541–557 (2014).

55. Arancibia-Cárcamo, I. L. *et al.* Node of ranvier length as a potential regulator of myelinated axon conduction speed. *eLife* **6**, e23329, DOI: 10.7554/eLife.23329 (2017).

56. Kandel, E. R. *et al.* *Principles of neural science*, vol. 4 (McGraw-hill New York, 2000).

57. Kim, S.-S. Finite difference time domain (fdtd) solver introduction (2022).

58. Nolte, J. The human brain: an introduction to its functional anatomy. 4th. *St Louis, MO: Mosby* (2008).

59. Zhuravlev, A., Tsvylev, O. & Zubkova, S. [spontaneous endogenous ultraweak luminescence of rat liver mitochondria in conditions of normal metabolism]. *Biofizika* **18**, 1037—1040 (1973).

60. Tuszyński, J. A. & Dixon, J. M. Quantitative analysis of the frequency spectrum of the radiation emitted by cytochrome oxidase enzymes. *Phys. Rev. E* **64**, 051915, DOI: 10.1103/PhysRevE.64.051915 (2001).

61. Mazhul', V. & Shcherbin, D. Phosphorescence analysis of lipid peroxidation products in liposomes. *BIOPHYSICS-PERGAMON THEN MAIK NAUKA-C/C OF BIOFIZIKA* **44**, 656–661 (1999).

62. Stoler, O. *et al.* Frequency- and spike-timing-dependent mitochondrial ca^{2+} signaling regulates the metabolic rate and synaptic efficacy in cortical neurons. *eLife* **11**, e74606, DOI: 10.7554/eLife.74606 (2022).

63. Albrecht-Buehler, G. Cellular infrared detector appears to be contained in the centrosome. *Cell motility cytoskeleton* **27**, 262–271 (1994).

64. Kato, M. Cytochrome oxidase is a possible photoreceptor in mitochondria. *Photobiochem Photobiophys* **2**, 263–269 (1981).

65. Wade, P. D., Taylor, J. & Siekevitz, P. Mammalian cerebral cortical tissue responds to low-intensity visible light. *Proc. Natl. Acad. Sci. - PNAS* **85**, 9322–9326 (1988).

66. Leszkiewicz, D. N., Kandler, K. & Aizenman, E. Enhancement of nmda receptor-mediated currents by light in rat neurones in vitro. *The J. physiology* **524**, 365–374 (2000).

67. Vandewalle, G., Maquet, P. & Dijk, D.-J. Light as a modulator of cognitive brain function. *Trends cognitive sciences* **13**, 429–438 (2009).

68. Starck, T. & Nissil, J. Stimulating brain tissue with bright light alters functional connectivity in brain at the resting state. (2012).

69. Zhang, K. X. *et al.* Violet-light suppression of thermogenesis by opsin 5 hypothalamic neurons. *Nat. (London)* **585**, 420–425 (2020).

70. Schmitt, F. O. & Bear, R. S. The ultrastructure of the nerve axon sheath. *Biol. Rev.* **14**, 27–50 (1939).

71. Schmitt, F. O. & Bear, R. S. The optical properties of vertebrate nerve axons as related to fiber size. *J. cellular comparative physiology* **9**, 261–273 (1937).

72. Adams, B. & Petruccione, F. Quantum effects in the brain: A review. (2019).

73. Fisher, M. P. Quantum cognition: The possibility of processing with nuclear spins in the brain. *Annals physics* **362**, 593–602 (2015).

74. Fedorov, A. K., Gisin, N., Beloussov, S. M. & Lvovsky, A. I. Quantum computing at the quantum advantage threshold: a down-to-business review. (2022).

75. Marshall, I. Consciousness and bose-einstein condensates. *New ideas psychology* **7**, 73–83 (1989).

76. Xu, J., Xu, Y., Sun, W., Li, M. & Xu, S. Experimental and computational studies on the basic transmission properties of electromagnetic waves in softmaterial waveguides. *Sci. reports* **8**, 13824–11 (2018).

77. Schubert, N., Axer, M., Pietrzyk, U. & Amunts, K. 3d polarized light imaging portrayed: Visualization of fiber architecture derived from 3d-pli. In Halefoğlu, A. M. (ed.) *High-Resolution Neuroimaging*, chap. 3, DOI: 10.5772/intechopen.72532 (IntechOpen, Rijeka, 2017).

78. Menzel, M. *et al.* A jones matrix formalism for simulating three-dimensional polarized light imaging of brain tissue. *J. Royal Soc. interface* **12**, 20150734–20150734 (2015).

79. Galvez, E. J. *et al.* Decoherence of photon entanglement by transmission through brain tissue with alzheimer's disease. *Biomed. optics express* **13**, 6621–6630 (2022).

80. Mamani, S. *et al.* Transmission of classically entangled beams through mouse brain tissue. *J. biophotonics* **11**, e201800096–n/a (2018).

81. Wirdatmadja, S. *et al.* Analysis of light propagation on physiological properties of neurons for nanoscale optogenetics. *IEEE Transactions on Neural Syst. Rehabil. Eng.* **27**, 108–117 (2019).

82. Nakahara, J., Maeda, M., Aiso, S. & Suzuki, N. Current concepts in multiple sclerosis: Autoimmunity versus oligodendrogliopathy. *Clin. reviews allergy immunology* **42**, 26–34 (2012).

83. Black, R. J. *Optical waveguide modes polarization, coupling, and symmetry* (McGraw-Hill, New York, 2010).

84. Yirmiyahu, Y., Niv, A., Biener, G., Kleiner, V. & Hasman, E. Excitation of a single hollow waveguide mode using inhomogeneous anisotropic subwavelength structures. *Opt. express* **15**, 13404–13414 (2007).

85. Chinn, P. & Schmitt, F. O. On the birefringence of nerve sheaths as studied in cross sections. *J. cellular comparative physiology* **9**, 289–296 (1937).

86. Bear, R. S. & Schmitt, F. O. Optical properties of the axon sheaths of crustacean nerves. *J. cellular comparative physiology* **9**, 275–287 (1937).

87. de Campos Vidal, B., Mello, M. L. S., Caseiro-Filho, A. C. & Godo, C. Anisotropic properties of the myelin sheath. *Acta histochemica* **66**, 32–39 (1980).

88. Kim, S.-S. Matrix transformation - simulation object (2020).

LaTeX formats citations and references automatically using the bibliography records in your .bib file, which you can edit via the project menu. Use the cite command for an inline citation

For data citations of datasets uploaded to e.g. *figshare*, please use the `howpublished` option in the bib entry to specify the platform and the link, as in the `Hao:gidmaps:2014` example in the sample bibliography file.

Acknowledgements (not compulsory)

Acknowledgements should be brief, and should not include thanks to anonymous referees and editors, or effusive comments. Grant or contribution numbers may be acknowledged.

Author contributions statement

Must include all authors, identified by initials, for example: A.A. conceived the experiment(s), A.A. and B.A. conducted the experiment(s), C.A. and D.A. analysed the results. All authors reviewed the manuscript.

Include credits of drawn diagrams here to fit Scientific Reports requirements !!

Additional information

To include, in this order: **Accession codes** (where applicable); **Competing interests** (mandatory statement).

The corresponding author is responsible for submitting a competing interests statement on behalf of all authors of the paper. This statement must be included in the submitted article file.

Figures and tables can be referenced in LaTeX using the ref command, e.g. Figure **??** and Table **??**.

A Myelin sheath modes

We examine the guided modes for the myelinated axon model. As described in a previous study simulating optical modes in the myelin sheath[13], guided modes obey the eigenmode wave equation as shown in Equation 1) for the boundary conditions applied by its waveguide, in this case the (homogeneous) myelin sheath. As laid out in a prior simulation study[13] considering myelin sheath modes, the solution of the wave equation $\vec{E}$ and its eigenvalue λ_e are as stated in Equation 2 – where z is the propagation axis, ω the angular frequency, ε the relative dielectric constant, μ the relative magnetic permeability, and k_z the longitudinal propagation constant. The propagation constant $k_z = \beta - i\alpha$ is composed of a phase constant β and an attenuation constant α. A guided mode that transmits along the myelin sheath must satisfy (1) $\alpha > 0$ such that the electric field intensity decreases with increased z indicating the wave travels forwards; and (2) $k_0 n_{int} < \beta < k_0 n_m$ where $k_0 = \frac{2\pi}{\lambda}$ is the vacuum propagation constant, such that light outside the waveguide is an attenuation wave and light within the waveguide achieves sufficient power for long-distance propagation.
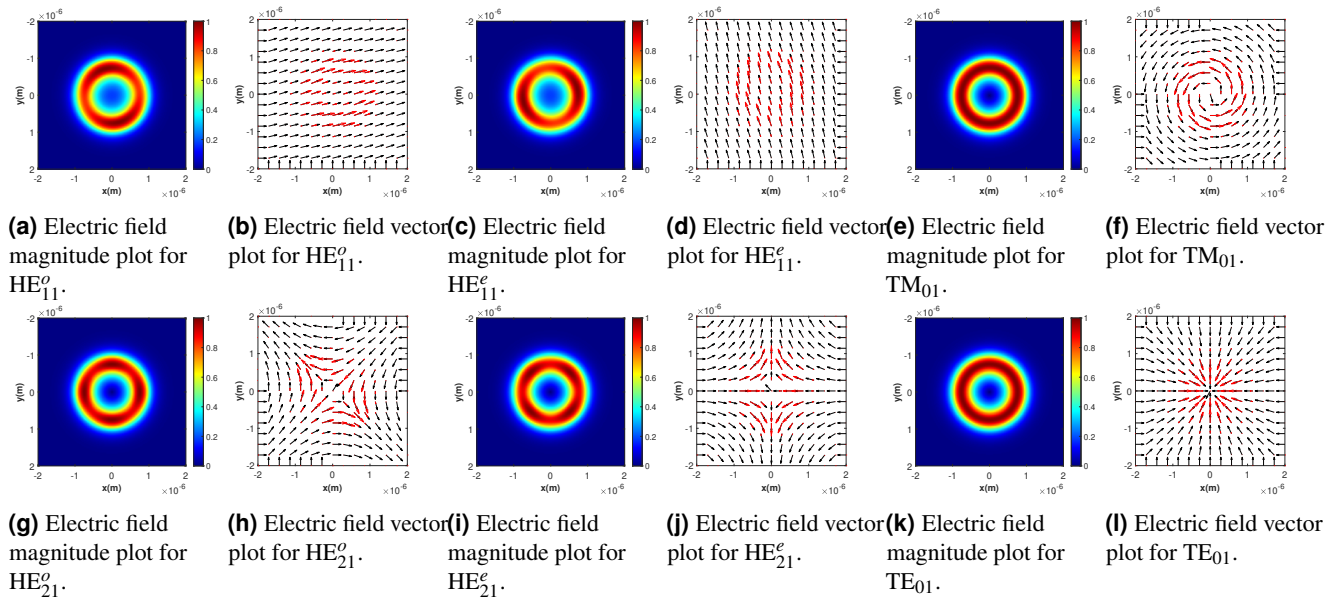
$$\nabla^2 \vec{E}(\vec{r},t) + \lambda_e \vec{E}(\vec{r},t) = 0$$
$$\nabla^2 \vec{H}(\vec{r},t) + \lambda_e \vec{H}(\vec{r},t) = 0 \tag{1}$$

$$\vec{E}(\vec{r},t) = \vec{E}(x,y) e^{i(\omega t - k_z t)}$$
$$\lambda_e = \omega^2 \varepsilon \mu - k_z^2 \tag{2}$$

We calculate the first twelve modes of the cross-section of our myelinated axon structure, ordered according to decreasing effective index. Electric field magnitude and vector plots for the first six modes are shown in Fig. 5, the next six modes are shown in Supplemental Information. Modes are labelled according to established convention for circular isotropic optical fibers.[13,83,84] For each mode we also record and discuss its effective index $n_{eff} = \frac{\beta}{k_0}$ (to four decimal places), which is analogous to its eigenvalue. For all modes we see that the electric field is well-confined to the myelin sheath (centered on the origin, inner radius of $0.6\,\mu$m, outer radius of $1\,\mu$m).

Most of the modes have magnitude plots which alternate between brighter, high-magnitude areas we refer to as anti-nodes, and dimmer, lower-magnitude areas which we will refer to as nodes. These modes do not have cylindrical symmetry, however this is expected as they are degenerate (sharing an effective index) and can thus be sorted into pairs related by a simple rotation. HE_{11}^o (Fig. 5a – 5b) and HE_{11}^e (Fig. 5c – 5d) have roughly linear polarization patterns and an effective index of $n_{eff} = 1.4412$. They each have two anti-nodes and two nodes, and they are related by a 90-degree rotation. HE_{21}^o (Fig. 5g – 5h) and HE_{21}^e (Fig. 5i – 5j) have roughly hyperbolic polarization patterns and an effective index of $n_{eff} = 1.4082$. They each have four anti-nodes and four nodes, and they are related by a 45-degree rotation. We also observe two modes with cylindrical symmetry which are non-degenerate. They have magnitudes equally distributed through the ring of the myelin sheath, without any anti-nodes or nodes. TM_{01} (Fig. 5e – 5f) has azimuthal polarization and an effective index of $n_{eff} = 1.4090$. TE_{01} (Fig. 5k – 5l) has radial polarization and an effective index of $n_{eff} = 1.4071$.

(a) Electric field magnitude plot for HE_{11}^o.

(b) Electric field vector plot for HE_{11}^o.

(c) Electric field magnitude plot for HE_{11}^e.

(d) Electric field vector plot for HE_{11}^e.

(e) Electric field magnitude plot for TM_{01}.

(f) Electric field vector plot for TM_{01}.

(g) Electric field magnitude plot for HE_{21}^o.

(h) Electric field vector plot for HE_{21}^o.

(i) Electric field magnitude plot for HE_{21}^e.

(j) Electric field vector plot for HE_{21}^e.

(k) Electric field magnitude plot for TE_{01}.

(l) Electric field vector plot for TE_{01}.

Figure 5. The first six modes calculated by the software (as ordered by decreasing effective index), named according to established convention[13,83,84]. Modes are calculated over the cross-section of the model at the source ($z = 0\,\mu$m). Input light amplitude is $1\,$V/m. Plots (a), (c), (e), (g), (i), (k) depict electric field magnitude. Electric field magnitudes given in units of V/m. Plots (b), (d), (f), (h), (j), (l) depict electric field vectors; black lines depict the normalized three-dimensional electric field vector at a given position, red arrows depict the magnitude-scaled three-dimensional electric field vector at a given position. The E_z component is negligible in all cases, on the order of $10^{-17}\,$V/m or less.

B Investigation of myelin sheath birefringence

B.1 Methods

When we investigate the effect of myelin sheath birefringence, the axon and interstitial fluid have the same optical properties as above, however the myelin sheath is modelled as a dielectric with positive birefringence along radial optical axes. The positive radial birefringence of the myelin sheath, known to be due to radial arrangement of lipid molecules[85–87], has been measured with a magnitude of $b = 0.011$[70,71]. While this magnitude was measured for fibers $10\,\mu$m $- 20\,\mu$m in myelin diameter, it was noted that findings of lower birefringence magnitude for smaller fibers may be due to the dominance of unmyelinated fibers of this size in the peripheral nervous system[70,71]. So we specify a refractive index matrix for the myelin sheath in cylindrical coordinates with diagonal elements $n_{rr} = 1.451$, $n_{\phi\phi} = 1.440$, $n_{zz} = 1.440$. The refractive index matrix for the myelin in cylindrical coordinates is as shown in Equation 3.

$$n_{m,cyl} = \begin{pmatrix} n_{rr} & 0 & 0 \\ 0 & n_{\phi\phi} & 0 \\ 0 & 0 & n_{zz} \end{pmatrix} = \begin{pmatrix} 1.451 & 0 & 0 \\ 0 & 1.44 & 0 \\ 0 & 0 & 1.44 \end{pmatrix} \tag{3}$$

For a given material the software allows the user to input a diagonal refractive index matrix and a transformation matrix.[88] The transformation matrix matrix Q specifies any coordinate transformation needed to rewrite the diagonal refractive index matrix n_{diag} in Cartesian coordinates, in the form of Equation 4, which is necessary as the software runs simulations in the Cartesian coordinate system.

$$n_{Cart} = Q^\dagger n_{diag} Q \tag{4}$$

Axon and interstitial fluid regions have already been set to uniform refractive indices, not requiring any coordinate transformation, so Q in these areas will be set to the identity matrix. For each point in the region of the myelin sheath, the transformation matrix Q_m should transform cylindrical to Cartesian coordinates. The columns of Q_m are the three cylindrical unit vectors $\hat{r}$, $\hat{\phi}$, and $\hat{z}$

written in Cartesian coordinates as shown in Equation 5.

$$Q_m = \begin{pmatrix} \hat{r} & \hat{\phi} & \hat{z} \end{pmatrix} = \begin{pmatrix} \cos\phi & -r\sin\phi & 0 \\ \sin\phi & r\cos\phi & 0 \\ 0 & 0 & 1 \end{pmatrix} \tag{5}$$

where $\phi = atan2\left(\frac{y}{x}\right)$ is the counter-clockwise angle from the +x axis

The matrix Q is defined at each point in a uniform grid laid across the cross-section of the model and centered on the z axis. (It is sufficient to define Q over a cross-sectional plane since the cylindrical-Cartesian coordinate transformation has no z dependence.) This grid samples 801 points within a $2\,\mu$m distance along the x axis, similarly it samples 801 points within a $2\,\mu$m distance along the y axis. (Outside this $2\,\mu$mx$2\,\mu$m cross-section is only more interstitial fluid within the simulation region, the matrix Q is set to the identity matrix by default.) For grid points within the myelin sheath, having distances r from the z axis that satisfy $r_a < r < r_m$, Q is set to Q_m. By specifying the diagonal refractive index matrix for myelin $n_{m,cyl}$ (which is in cylindrical coordinates) and the appropriate transformation matrix Q_m which converts from cylindrical to Cartesian coordinates, the software processes the Cartesian refractive index matrix for myelin as shown in Equation 6.

$$n_{m,Cart} = Q^{\dagger} n_{m,cyl} Q = \begin{pmatrix} n_{rr}\cos^2\phi + n_{\phi\phi}\sin^2\phi & \left(n_{\phi\phi} - n_{rr}\right)\cos\phi\sin\phi & 0 \\ \left(n_{\phi\phi} - n_{rr}\right)\cos\phi\sin\phi & n_{rr}\sin^2\phi + n_{\phi\phi}\cos^2\phi & 0 \\ 0 & 0 & n_{zz} \end{pmatrix} \tag{6}$$

The elements refractive index matrix of the entire 2μm x 2μm cross-section can be seen with respect to position in Figure 6. In the regions of the axon and the interstitial fluid, their uniform indices ($n_a = 1.38$ and $n_{int} = 1.34$ respectively) are constant in the diagonal elements and zero in off-diagonal elements. In the region of the myelin sheath, the refractive index varies due to the nonzero birefringence magnitude in the xx, xy, yx, and yy matrix elements.
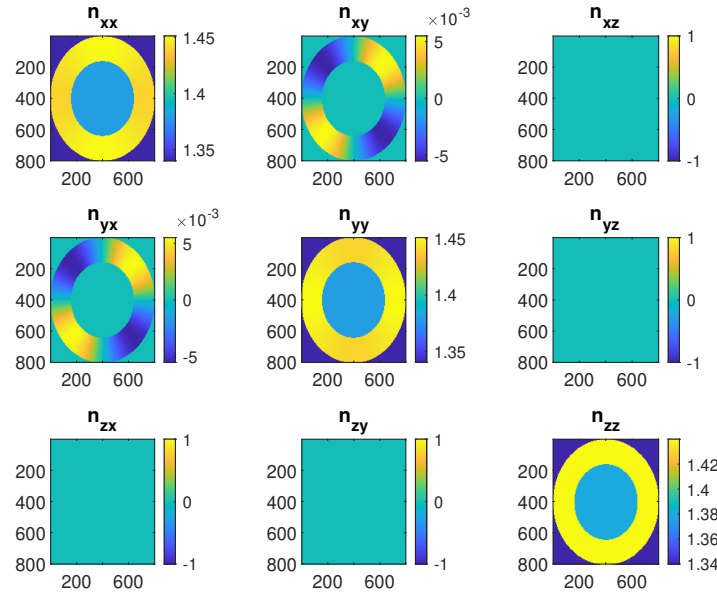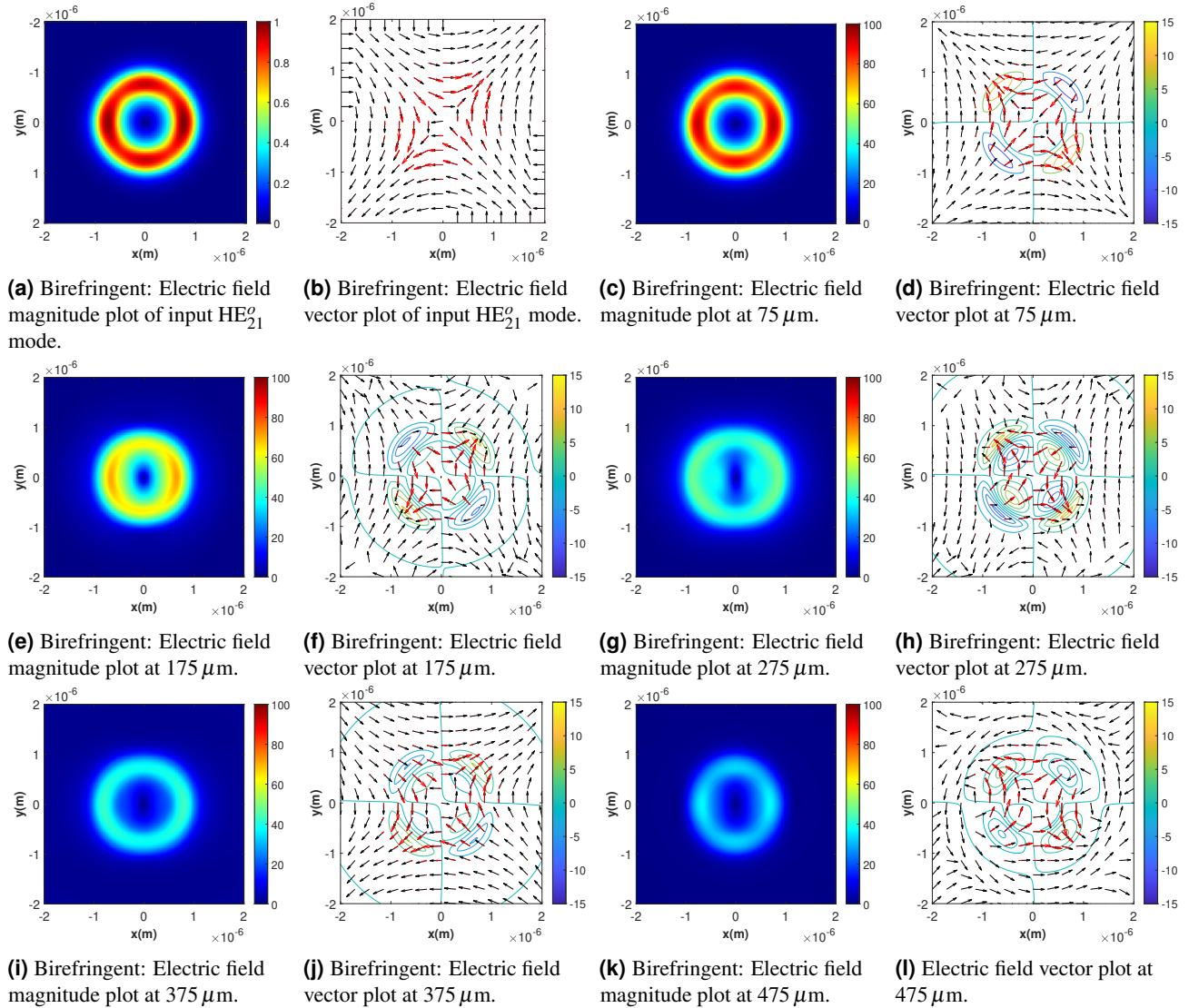

Figure 6. Refractive index matrix elements in Cartesian coordinates as a function of position in units of sample point. Resolution is 801 sample points to $2\,\mu$m. In physical units, horizontal and vertical axes each run from -1 μm to 1 μm. Color gradient indicates differences in refractive index. This depicts the radial birefringence of myelin, the radial refractive index value is $n = 1.451$ whereas in other directions $n = 1.440$. Note refractive index for the surrounding fluid $n = 1.34$ and for the axon $n = 1.38$.

B.2 Results

At 75 μm the electric field profiles within the homogeneous and birefringent models are shown in Fig. 3c – 3d and Fig. 7c – 7d respectively. The modes are transmitting ideally within the myelin sheath, with 100% transmission as shown in Fig. 8. The electric field vector plot still features a hyperbolic polarization pattern, consistent with the input modes, so there is no apparent change from myelin sheath birefringence. We recognize that out of the four (high-magnitude) anti-nodes in the birefringent

mode shown in Fig. 7a, the left-right anti-nodes are slightly larger than than the top-bottom anti-nodes in contrast to the equal anti-nodes for the homogeneous mode in Fig. 3a. This effect is exaggerated at $175\,\mu$m, after the light has travelled through the first Ranvier node. Here the homogeneous model has evenly distributed electric field in Fig. 3e, however for the birefringent model in Fig. 7e we see higher electric field magnitude on the left-right sides of the myelin sheath. There is also clearly an overall drop in electric field magnitude due to transmission loss at the first Ranvier node. As shown in Fig. 3f and Fig. 7f, the electric field vectors still form a hyperbolic polarization pattern. These qualities are also observed at $275\,\mu$m, shown in Fig. 3g – 3h and Fig. 7g – 7h, as well as at $475\,\mu$m, shown in Fig. 3k – 3l and Fig. 7k – 7l. The overall electric field magnitude drops as the light travels through more Ranvier nodes, the birefringent model has higher magnitude on the left-right sides in comparison to the top-bottom sides of the myelin sheath, and the hyperbolic polarization pattern within the sheath appears mostly conserved.

(a) Birefringent: Electric field magnitude plot of input HE_{21}^{o} mode.

(b) Birefringent: Electric field vector plot of input HE_{21}^{o} mode.

(c) Birefringent: Electric field magnitude plot at $75\,\mu$m.

(d) Birefringent: Electric field vector plot at $75\,\mu$m.

(e) Birefringent: Electric field magnitude plot at $175\,\mu$m.

(f) Birefringent: Electric field vector plot at $175\,\mu$m.

(g) Birefringent: Electric field magnitude plot at $275\,\mu$m.

(h) Birefringent: Electric field vector plot at $275\,\mu$m.

(i) Birefringent: Electric field magnitude plot at $375\,\mu$m.

(j) Birefringent: Electric field vector plot at $375\,\mu$m.

(k) Birefringent: Electric field magnitude plot at $475\,\mu$m.

(l) Electric field vector plot at $475\,\mu$m.

Figure 7. In the case of the birefringent myelin sheath model: Electric field profiles of calculated input mode HE_{21}^{o} and cross-sections of the four-Ranvier-node myelinated axon structure at positions $75, 175, 275, 375, 475\,\mu$m. The mode source is located at $0\,\mu$m, input amplitude is $100\,$V/m. Ranvier nodes are $2\,\mu$m long and begin at $z = 100, 200, 300, 400\,\mu$m. Plots (a), (c), (e), (g), (i), (k) depict electric field magnitude. Plots (b), (d), (f), (h), (j), (l) depict electric field vectors; black lines depict the normalized three-dimensional electric field vector at a given position, red arrows depict the magnitude-scaled three-dimensional electric field vector at a given position; color-coded contour lines depict magnitude of E_z. Electric field magnitudes given in units of V/m.

The transmission coefficient T was recorded every $25\,\mu$m along the length of the myelin sheath, for the cross-sectional area of the simulation region ($4\,\mu$m x $4\,\mu$m). The natural log of the transmission coefficient T is plotted against the length of the myelin sheath in Fig. 8, which has plotting the homogeneous model in blue and the birefringent model in red. We see perfect transmission through each of the models prior to $100\,\mu$m. The four decreases in transmission occur just beyond the positions of the four Ranvier nodes at $z = 100, 200, 300, 400\,\mu$m. This transmission loss is very similar between models, we do see slightly greater transmission loss for the birefringent model. Again, both models show higher than expected transmission based on the assumption of exponentiated transmission loss through the multiple Ranvier nodes.
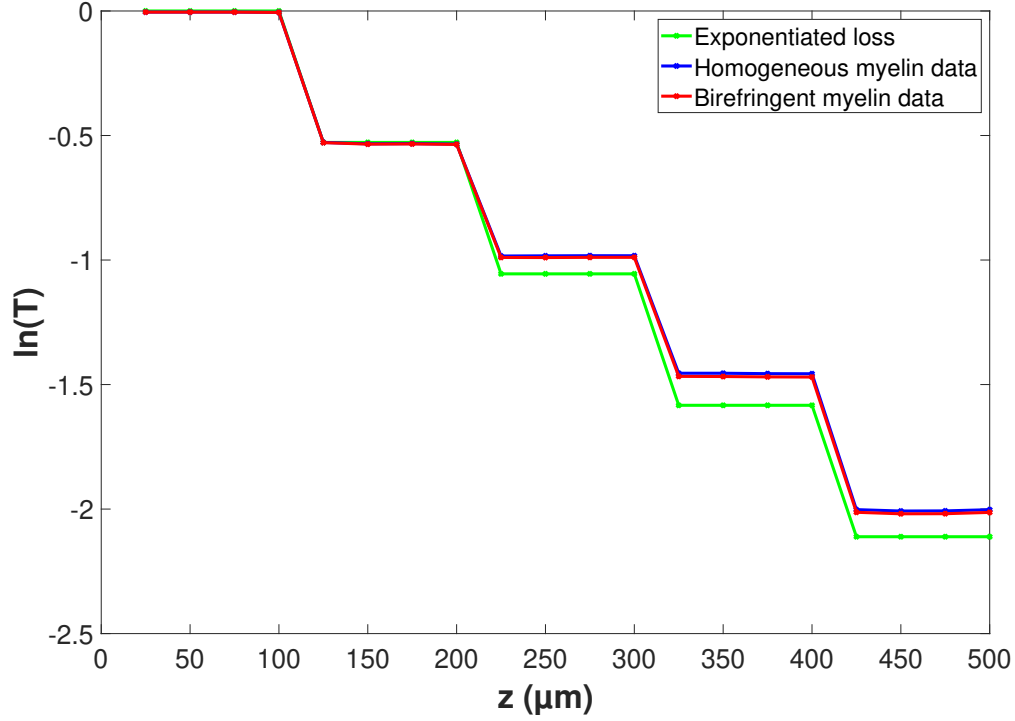
Figure 8. Natural log of transmission coefficient T as a function of distance z along the four-Ranvier-node myelinated axon structure. The blue line shows transmission data from the simulation for the case of homogeneous myelin sheath; the green line shows transmission data expected from the assumption of exponentiated loss through each Ranvier node, using the measured transmission loss from the first Ranvier node in the case of the homogeneous myelin sheath; the red line shows transmission data from the simulation for the case of the birefringent myelin sheath. The mode source is located at $z = 0\,\mu$m, Ranvier nodes are $2\,\mu$m long and begin at $z = 100, 200, 300, 400\,\mu$m.